

Realizing repeated quantum error correction in a distance-three surface code

<https://doi.org/10.1038/s41586-022-04566-8>

Received: 15 November 2021

Accepted: 9 February 2022

Published online: 25 May 2022

 Check for updates

Sebastian Krinner^{1,9}, Nathan Lacroix^{1,9}, Ants Remm¹, Agustin Di Paolo^{2,3}, Elie Genois^{2,3}, Catherine Leroux^{2,3}, Christoph Hellings¹, Stefania Lazar¹, Francois Swiadek¹, Johannes Herrmann¹, Graham J. Norris¹, Christian Kraglund Andersen^{1,8}, Markus Müller^{4,5}, Alexandre Blais^{2,3,6}, Christopher Eichler¹ & Andreas Wallraff^{1,7}

Quantum computers hold the promise of solving computational problems that are intractable using conventional methods¹. For fault-tolerant operation, quantum computers must correct errors occurring owing to unavoidable decoherence and limited control accuracy². Here we demonstrate quantum error correction using the surface code, which is known for its exceptionally high tolerance to errors^{3–6}. Using 17 physical qubits in a superconducting circuit, we encode quantum information in a distance-three logical qubit, building on recent distance-two error-detection experiments^{7–9}. In an error-correction cycle taking only 1.1 μs , we demonstrate the preservation of four cardinal states of the logical qubit. Repeatedly executing the cycle, we measure and decode both bit-flip and phase-flip error syndromes using a minimum-weight perfect-matching algorithm in an error-model-free approach and apply corrections in post-processing. We find a low logical error probability of 3% per cycle when rejecting experimental runs in which leakage is detected. The measured characteristics of our device agree well with a numerical model. Our demonstration of repeated, fast and high-performance quantum error-correction cycles, together with recent advances in ion traps¹⁰, support our understanding that fault-tolerant quantum computation will be practically realizable.

The surface code^{4,11} is a planar realization of Kitaev's toric code³, which uses topological features of a qubit lattice to correct errors in quantum information-processing systems. This code is a prominent contender to reach fault-tolerant quantum computation because of its high error threshold of about 1% against quantum circuit noise^{5,12} and its compatibility with 2D architectures. The surface code belongs to the family of stabilizer codes^{13,14}, which encode quantum information into a joint subspace of definite parities on a set of physical data qubits to form a logical qubit. Errors are detected using measurements of auxiliary qubits to extract parity information without collapsing the logical qubit state. The fault-tolerant operation of a quantum computer requires repeated detection and correction of both bit-flip and phase-flip errors on data qubits. With an increasing number of physical qubits and thus an increasing code distance d , the number of errors $\lfloor (d-1)/2 \rfloor$ that can at least be detected and corrected per error-correction cycle increases, making the code more resilient when error rates are sufficiently low.

Error correction limited to a single type of error has been realized with repetition codes in nuclear magnetic resonance¹⁵, trapped ions¹⁶, nitrogen-vacancy centres¹⁷ and superconducting circuits^{9,18}. In single-cycle experiments, fault-tolerant stabilizer measurements and correction of both types of error have been demonstrated with the five-qubit code and the Bacon–Shor code^{19–22}. Recently, error detection in a distance-two surface code has been realized with seven qubits^{7–9},

and only very recently, repeated stabilizer-based error correction has been demonstrated with a distance-three colour code in a trapped-ion system¹⁰.

Correction of both bit-flip and phase-flip errors requires at least a distance-three code. In combination with fault-tolerant circuits for error-syndrome measurements, this guarantees that any single error on any of the constituent data and auxiliary qubits or operations can be corrected^{14,23}. While the work we discuss here focuses on digital encoding of quantum information, continuous-variable encoding, for example, in harmonic oscillator states, constitutes an alternative approach to quantum error correction; see, for example, refs. ^{24–27}.

Realization in superconducting circuits

Experimentally realizing a distance-three surface code requires nine data qubits and eight auxiliary qubits^{23,28,29}, also referred to in the literature as ancilla or measurement qubits. The qubits are arranged in a diagonal, planar square lattice, the edges of which are shown in grey in the schematic of Fig. 1a. The data qubits $D_j, j = 1 \dots 9$ (red dots) form a 3×3 array and are interlaced with auxiliary qubits A_i , labelled X_i (blue) and $Z_i, i = 1 \dots 4$ (green). We realized this arrangement in a superconducting circuit using 17 transmon qubits³⁰ (yellow) capacitively coupled to each other along the edges of the square array with roughly 1-mm-long

¹Department of Physics, ETH Zurich, Zurich, Switzerland. ²Institut Quantique, Université de Sherbrooke, Sherbrooke, Québec, Canada. ³Département de Physique, Université de Sherbrooke, Sherbrooke, Québec, Canada. ⁴Institute for Quantum Information, RWTH Aachen University, Aachen, Germany. ⁵Peter Grünberg Institute, Theoretical Nanoelectronics, Forschungszentrum Jülich, Jülich, Germany. ⁶Canadian Institute for Advanced Research, Toronto, Ontario, Canada. ⁷Quantum Center, ETH Zurich, Zurich, Switzerland. ⁸Present address: QuTech and Kavli Institute for Nanoscience, Delft University of Technology, Delft, The Netherlands. ⁹These authors contributed equally: Sebastian Krinner, Nathan Lacroix. [✉]e-mail: skrinner@phys.ethz.ch

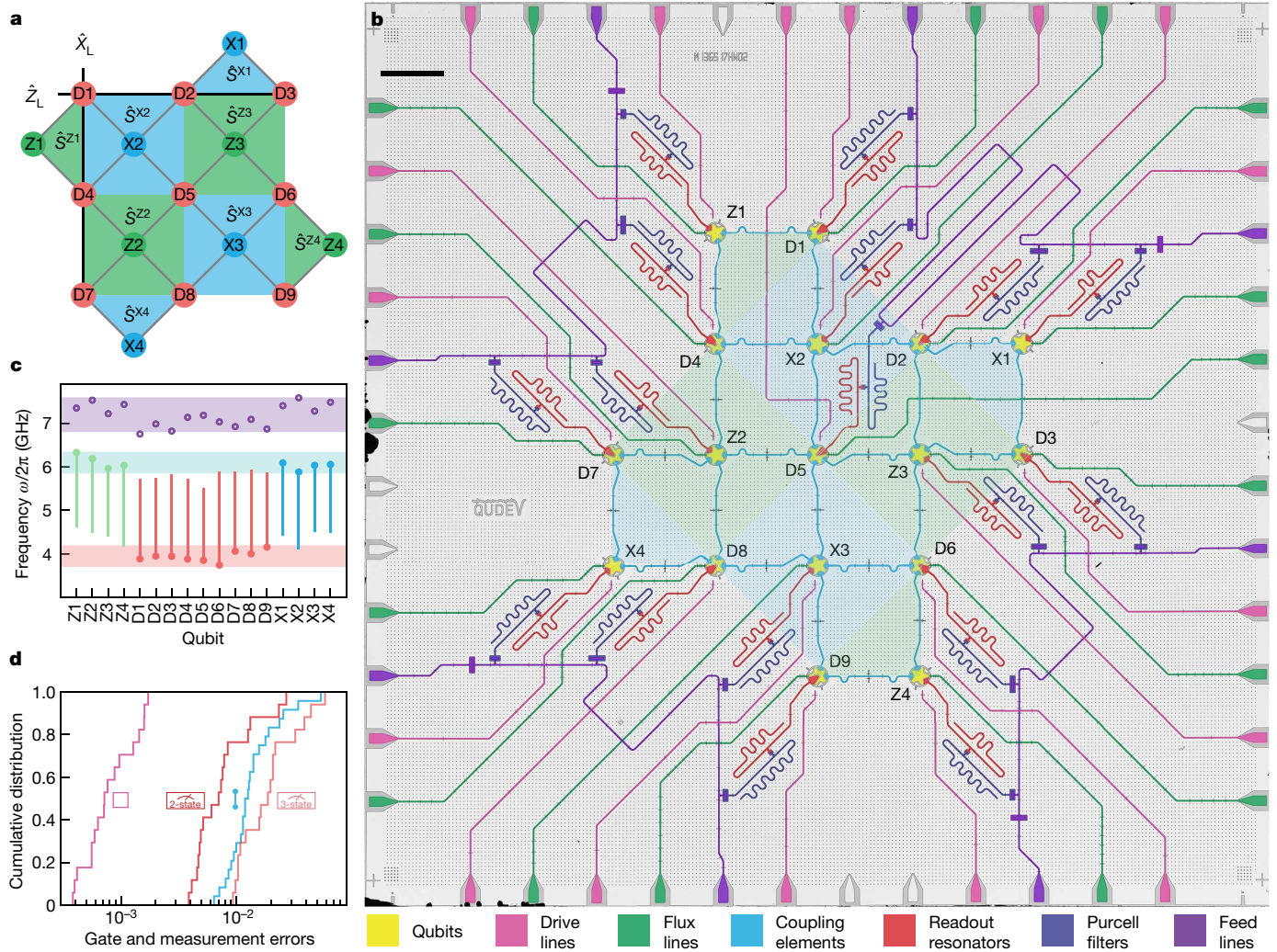


Fig. 1 | Device concept, architecture and performance. **a**, Conceptual representation of the distance-three surface code consisting of data qubits (red circles), Z-type auxiliary qubits (green circles) and X-type auxiliary qubits (blue circles), with their connectivity indicated by grey lines. The data qubits participating in the weight-three logical operators \hat{Z}_L and \hat{X}_L are indicated by solid black lines. Green (blue) plaquettes indicate X-type (Z-type) stabilizer circuits. **b**, False-colour micrograph of the device realizing the concept in **a** with 17 transmon qubits; see key for circuit elements and text for details. The

qubit lattice is rotated by 45° with respect to **a**. The scale bar denotes 1 mm. **c**, Frequency arrangement in three distinct bands for idling data qubits (red circles), idling Z-type/X-type auxiliary qubits (green/blue circles) and readout resonators (violet open circles). The qubit-frequency tuning ranges are indicated by vertical bars. **d**, Cumulative distributions (integrated histograms) of single-qubit gate (pink), simultaneous two-qubit gate (cyan), and two-state (red) and three-state readout errors (light red).

coplanar waveguide segments (cyan); see Fig. 1b. We discuss the fabrication of this device in the Supplementary Information (section I).

Using the auxiliary qubits X_i and Z_i , we measure the parity of the neighbouring two or four data qubits D_j , which are located at the vertices of the blue and green plaquettes (Fig. 1a, b), in the X or Z basis, see Methods. These parity measurements are also referred to as stabilizer measurements^{13,14}. The corresponding mutually commuting weight-two (or weight-four) stabilizer operators $\hat{S}^{X_i} = \prod_{j=1}^{2(4)} \hat{X}_j$ and $\hat{S}^{Z_i} = \prod_{j=1}^{2(4)} \hat{Z}_j$ of the surface code are products of two (or four) Pauli- \hat{X} or Pauli- \hat{Z} operators of the data qubits j located at the vertices of a given data-qubit plaquette. Measurements of the stabilizer operator \hat{S}^{A_i} with outcomes $s^{A_i} = \pm 1$ indicate even or odd parity of the corresponding data-qubit state. A change of data-qubit parity signals an error. In our experiments, in which we do not reset auxiliary qubits, odd parity is indicated by a change of auxiliary-qubit state from cycle to cycle, whereas even parity is indicated by the absence of such changes.

In our experiments, the stabilizer gate sequence is realized as two or four controlled-phase (CZ) gates^{31–33} (see Methods), between data

and auxiliary qubits, operated in a low and high frequency band (see Fig. 1c), respectively, combined with initial and final $\pi/2$ rotations on the auxiliary qubits (Fig. 2a, b). The gate sequence for measuring \hat{S}^{X_i} contains further initial and final $\pi/2$ rotations acting on the data qubits, implementing a basis change from the Z to the X basis (blue dashed squares in Fig. 2a, b). We apply echo pulses to the data qubits in the middle of the gate sequence to reduce dephasing of the data qubits and residual coherent coupling to spectator qubits³⁴.

The 24 pairwise CZ gates have a mean duration of 98(7) ns, including two conservatively chosen 15-ns-long buffers at the beginning and the end, and show a mean gate error of 0.015(10). The gate error histogram, shown as an integrated (cumulative) distribution, shows variations of about a factor of four in two-qubit gate error (Fig. 1d and Methods). Single-qubit gates showing a mean error of 0.0009(4) are realized by applying short resonant microwave pulses to each qubit individually through a dedicated drive line (pink coplanar waveguide in Fig. 1b). We determined both single-qubit and two-qubit gate fidelities in randomized benchmarking experiments. We discuss the experimental setup used to realize these gates in the Supplementary Information (section IV).

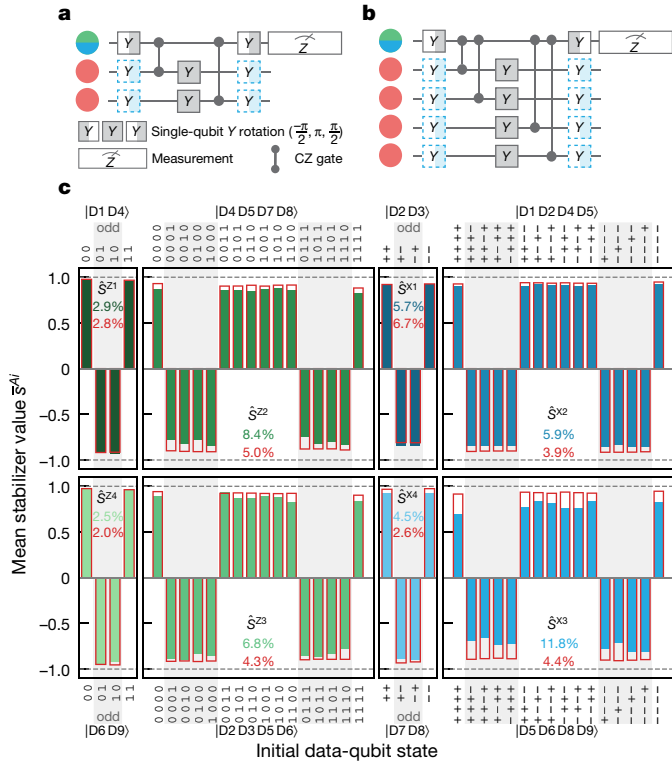


Fig. 2 | Stabilizer circuits and their characterization. Quantum circuit diagrams for weight-two (a) and weight-four (b) stabilizers acting between data qubits located on the vertices of a plaquette (red circles) and the corresponding auxiliary qubit used for Z-type (green circles) or X-type (blue circles) stabilizer measurements, in which the latter require a basis change (blue dashed squares); see text for details. c, Measured (filled bars) and simulated (red wireframes) average stabilizer values \bar{s}^{Ai} versus data-qubit input state, ordered by number of excitations. Percentages are the experimental (blue and green) and simulated (red) error of \bar{s}^{Ai} . Grey background indicates odd parity and white indicates even parity.

A key element of individual stabilizer measurements are fast and high-fidelity measurements of auxiliary-qubit states while leaving data-qubit states unaffected^{35–37}; see Methods. Accurate stabilizer measurements using mid-cycle qubit readout on timescales comparable with or shorter than the cumulated gate times per error-correction cycle also contribute to maximizing the performance of error detection and correction in our surface-code implementation as a whole.

With our readout scheme, we discriminate the two computational qubit states and a leakage state, which—if undetected or uncorrected for—is detrimental to any surface-code implementation^{37–42}. We achieve a mean readout assignment error of 0.009(7) when discriminating the computational states only (two-state readout) and of 0.022(14) when discriminating the computational states and the leakage state (three-state readout); see Supplementary Information (section VI). The corresponding cumulative distribution for two-state readout exhibits performance variations on the device of about a factor of two when disregarding two outliers, whereas the distribution for three-state readout shows variations larger by about a factor of two (Fig. 1d).

With all elements in place for realizing a surface code, we first characterize the measurements of individual \hat{S}^{Ai} stabilizers. To do so, we prepare the data qubits D_j of a given weight-two or weight-four plaquette sequentially in each one of its $2^2 = 4$ or $2^4 = 16$ basis states composed of $|0\rangle$ and $|1\rangle$ for \hat{S}^{Zi} and $|+\rangle$ and $|-\rangle$ for \hat{S}^{Xi} . At the beginning of each experiment, all qubits are initialized by heralding the ground state $|0\rangle$ from single-shot readout.

For each input state, we compute the mean values \bar{s}^{Ai} from about 4×10^4 measurements of s^{Ai} (coloured bars in Fig. 2c) and find good qualitative agreement with master equation simulations (red outlines); see Supplementary Information (sections VII and VIII) for details. Here $+1/-1$ indicate even/odd parity of the measured state. The coloured percentage values show the corresponding experimental and simulated errors of the stabilizer measurements. On average, the experimental parity assignment error is 3.9(1.3)% for weight-two stabilizers and 8.2(2.2)% for weight-four stabilizers. We attribute the differences between measurements and simulation mostly to two-qubit gate errors owing to microscopic defect modes changing their frequency on timescales of hours or days (Supplementary Information, section III).

Having verified that all stabilizer measurements perform at high quality levels individually, we combine the stabilizer measurements into a surface-code cycle. Executing this cycle once, we prepare one of the four cardinal logical qubit states. Executing the cycle several times, we stabilize the logical states and investigate the performance of our realization of the code.

The surface-code cycle

At the beginning of each experimental sequence, we prepare the nine data qubits in either one of the product states $|0\rangle^{\otimes 9}$ and $|\hat{X}_1|0\rangle^{\otimes 9}$ ($|+\rangle^{\otimes 9}$ and $|\hat{Z}_1|+\rangle^{\otimes 9}$) to begin the process of initializing the cardinal logical qubit states $|0\rangle_L$ and $|1\rangle_L$ ($|+\rangle_L$ and $|-\rangle_L$). The cardinal states are eigenstates of the eight stabilizer operators \hat{S}^{Ai} and ± 1 eigenstates of the logical Pauli operators, which we choose as $\hat{Z}_L = \hat{Z}_1\hat{Z}_2\hat{Z}_3$ and $\hat{X}_L = \hat{X}_1\hat{X}_4\hat{X}_7$; see solid black lines in Fig. 1a. As required, \hat{Z}_L and \hat{X}_L commute with all stabilizers and anti-commute with each other. Because each of the prepared product states is an equal superposition of 16 equivalent instances of the target logical state, executing a single quantum error-correction cycle deterministically initializes the target logical state in the stabilizer eigenspace corresponding to the measurement outcome of the stabilizers (Supplementary Information, section IX).

In a single surface-code cycle, we first execute all gate operations implementing the four \hat{S}^{Zi} stabilizer measurements. We realize the necessary two-qubit gates in four time steps, in each of which we execute three CZ gates simultaneously; see Methods. Parallelizing stabilizer execution is a key technical requisite for scalable quantum error correction, in particular for operation of larger-distance codes.

The gate execution is followed by readout of the Z-type auxiliary qubits to complete the Z-type stabilizer measurements; see Fig. 3a. Simultaneous with the Z-type auxiliary-qubit readout, we start executing the X-type stabilizer circuits, which are equivalent up to a basis change of the data qubits. This allows us to execute the \hat{S}^{Zi} and \hat{S}^{Xi} stabilizer measurements in a parallel, pipelined approach⁴³, which imposes fewer constraints on the choice of two-qubit gate interaction frequencies compared with parallel scheduling^{29,44}. See Fig. 3a for a full circuit diagram and Supplementary Information (section X) for a full pulse sequence. In the pipelined approach with fast readout, we achieve a short quantum error-correction cycle time of $t_c = 1.1 \mu\text{s}$. A short t_c relative to the physical qubit coherence times is essential to be able to identify errors unambiguously. Moreover, a short absolute value of t_c reduces the execution time of error-corrected quantum algorithms^{45,46}.

To maximize the performance of the distance-three surface code, we have designed our device with parameters minimizing leakage on data qubits. In addition, we reject all experimental runs with residual leakage events, which we detect on auxiliary qubits during the execution of each cycle and on data qubits after the last cycle, using our three-state readout; see Methods. We discuss the fraction of experimental runs retained after leakage rejection in the Supplementary Information (section XI).

To characterize the fidelity of the nine-data-qubit logical state that we initialized deterministically using our measurement-based approach, we measure the expectation values of the 2^9 Pauli operator

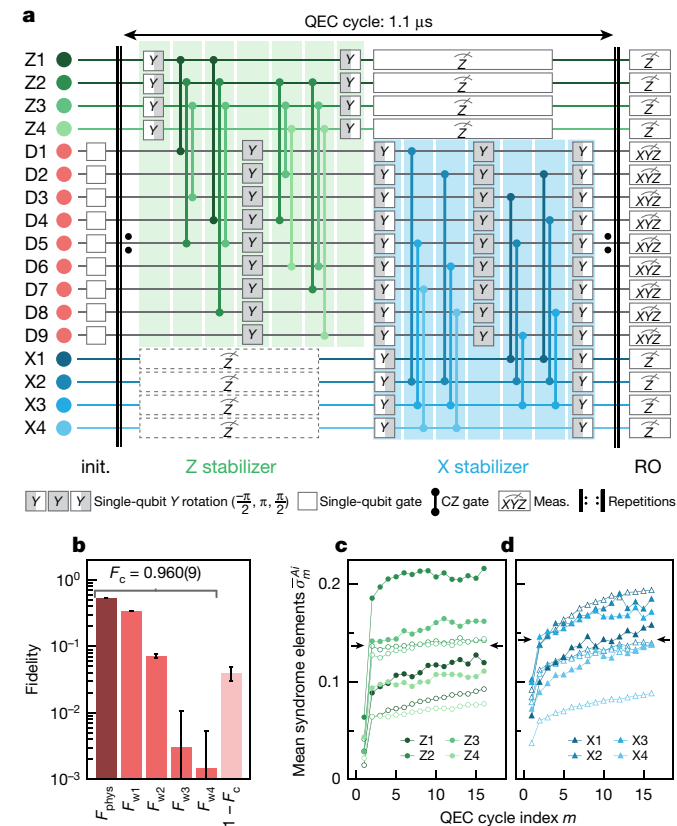


Fig. 3 | The surface-code cycle, fidelity of logical-state initialization and average error syndromes. **a**, Quantum circuit used to initialize and (repeatedly) error correct the distance-three surface code logical qubit. Green (blue) shaded circuit elements represent the parallel execution of the four Z-type (X-type) stabilizer circuits. Empty squares indicate single-qubit rotations on data qubits. In the first cycle, the X_i auxiliary qubits are not measured (dashed boxes). **b**, Fidelity of the prepared logical state $|0\rangle_L$ (dark red bar), all correctable states differing from $|0\rangle_L$ by one to four Pauli errors (red bars) and all uncorrectable states (light red bar). Fidelities are computed as the means over 500 different correctable subspaces (Supplementary Information, section IX) and error bars indicate one standard deviation. Average syndrome elements $\bar{\sigma}_m^{Ai}$ as a function of the cycle index m for the \hat{Z}_L (**c**, filled circles) and the \hat{X}_L (**d**, filled triangles) preservation experiment. Open symbols are simulations. The black arrows indicate the average syndrome element over all stabilizers and cycles; see text for details. QEC, quantum error correction.

strings that form the basis of the target state^{20,47}. For $|0\rangle_L$, we find a quantum state fidelity of $F_{\text{phys}} = \text{Tr}(\rho|0\rangle_L\langle 0|_L) = 54.0(1)\%$ (dark red bar in Fig. 3b). Considering only errors in the logical subspace⁷, we find a logical fidelity of $F_L = 99.6(2)\%$; see Methods and Supplementary Information (section IX). We also determine the fidelity of the experimentally prepared state with respect to correctable subspaces including states that are equivalent to the target state up to Pauli errors of weight $i = 1 \dots 4$ and find $(F_{w1}, F_{w2}, F_{w3}, F_{w4}) = [34.3(0), 7.3(5), 0.3(8), 0.1(4)]\%$. Hence the prepared initial state has a fidelity of $F_c = F_{\text{phys}} + \sum_{i=1}^4 F_{wi} = 96.0(9)\%$ with respect to states that are, in principle, correctable; see Supplementary Information (section IX).

Repeated quantum error correction

Once the first quantum error-correction cycle completes the logical-state initialization, we make use of all subsequent cycles for logical-state preservation. In our experiments, we preserve the cardinal logical qubit states for up to $n = 16$ cycles. In each cycle $m = 1 \dots n$, we extract eight stabilizer values σ_m^{Ai} . Changes in stabilizer values signal

the occurrence of errors and are used to construct error syndromes σ_m consisting of eight syndrome elements $\sigma_m^{Ai} = (1 - s_m^{Ai} \times s_{m-1}^{Ai})/2$. The elements σ_m^{Ai} are inferred in each cycle from the current (m) and the previous ($m - 1$) measured stabilizer values, with $\sigma_m^{Ai} = 1(0)$ indicating an error (no error)¹⁸.

We collectively process successive syndromes σ_m to determine which data and auxiliary qubits have most probably suffered an error^{4,14,44} using the approach described in Methods. Executing n consecutive error-correction cycles and rejecting runs in which leakage has been detected, we record stabilizer measurement outcomes and construct syndromes from their values, the averages of which are shown in Fig. 3c, d. When averaging the syndromes over all individual elements and time, we find that the average syndrome element $\bar{\sigma} = 0.14 \ll 1$ is small (see arrows in Fig. 3c, d), indicating that errors are rare and therefore allowing for efficient error detection and correction⁹. In Methods, we discuss the syndrome measurement outcomes in more detail.

To determine the performance of our distance-three surface code, we extract the logical error per cycle when preserving eigenstates of the logical qubit operators \hat{Z}_L and \hat{X}_L versus the number of executed cycles n . For each sequence of cycles, we decode the error syndromes, including a syndrome determined from the final data-qubit readout. We use a minimum-weight perfect-matching algorithm, the weights of which we determine in an error-model-free approach (Methods). After the n th cycle, we perform a projective readout of the final data-qubit state in the Z or X basis, from which we determine the eigenvalue $z_L = \pm 1$ of \hat{Z}_L or $x_L = \pm 1$ of \hat{X}_L .

Decoding the error syndromes and applying corrections to z_L or x_L when indicated (Methods), we compute the mean logical qubit expectation values $\bar{z}_L = \langle \hat{Z}_L \rangle$ and $\bar{x}_L = \langle \hat{X}_L \rangle$ as a function of n from a total of 10^6 experimental runs, in which the available data are reduced by ground-state heralding before and leakage rejection during each run. We observe an exponential decay of $\langle \hat{Z}_L \rangle$ and $\langle \hat{X}_L \rangle$ with n (solid symbols in Fig. 4a, b). From the logical qubit operator expectation values, we extract the logical error probability $\varepsilon_L = (1 - \langle \hat{Z}_L \rangle)/2$ (solid symbols in Fig. 4c) as a function of n and find a small logical error per cycle of $\varepsilon_L = [1 - \exp(-t_c/T_{2,L})]/2 \approx t_c/2T_{2,L} = 0.032(1)$, also indicated on the right-hand side of the corresponding dataset in Fig. 4c. Equivalently, we obtain $\varepsilon_L = [1 - \exp(-t_c/T_{2,L})]/2 \approx t_c/2T_{2,L} = 0.029(1)$ for $\langle \hat{X}_L \rangle$. We note that both the coherence time of $T_{2,L} = 18.2(5) \mu\text{s}$ and the lifetime $T_{1,L} = 16.4(8) \mu\text{s}$ of the logical qubit, as extracted from the decay curves of $\langle \hat{X}_L \rangle$ and $\langle \hat{Z}_L \rangle$ are much longer than the duration of the quantum error-correction cycle $t_c = 1.1 \mu\text{s}$ in our implementation of the surface code. For completeness, in the Supplementary Information (section XI) we, also state and discuss the logical error per cycle when leakage is not rejected.

We note that, in our implementation of the surface code, the logical coherence time is only about a factor of two lower than the mean physical coherence time $\bar{T}_2 = 37.5 \mu\text{s}$ of all 17 qubits, whereas the logical relaxation time is about a factor of four lower than twice the mean physical energy relaxation time $2\bar{T}_1 = 65.0 \mu\text{s}$, as indicated in Fig. 4a, b. We discuss this result further in Methods and put it into context in the next section.

Performance assessment and projection

We compare the state-preservation experiments with numerical simulations using a Monte Carlo wavefunction method (open symbols in Fig. 4a–c). The model underlying the simulations (Supplementary Information, section VII) uses the measured coherence times, interaction rates and readout errors of the device as inputs. We find that, despite the complexity of the quantum error-correction cycle, the measured expectation values $\langle \hat{X}_L \rangle$ and $\langle \hat{Z}_L \rangle$, when rejecting leakage, come close to the simulated values (open symbols in Fig. 4a, b). The logical lifetimes extracted from exponential fits (dashed lines in Fig. 4a, b) to the simulated expectation values are approximately $26 \mu\text{s}$. They

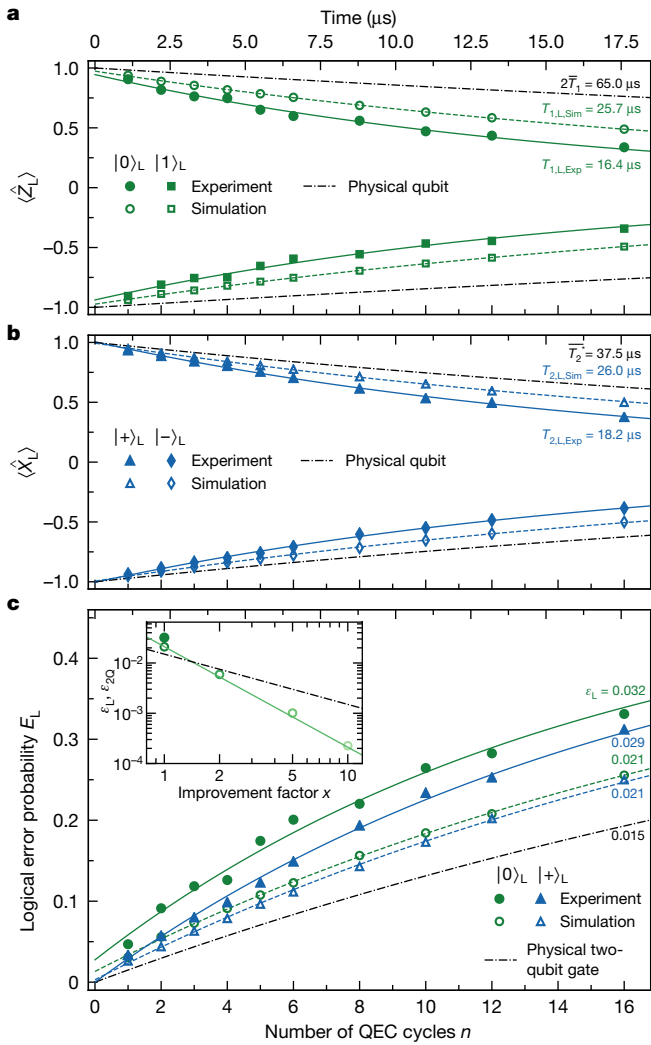


Fig. 4 | Logical-state preservation and error per cycle. **a**, Experimentally determined (full symbols) and simulated (open symbols) expectation value of the \hat{Z}_L operator for prepared $|0\rangle_L$ (circles) and $|1\rangle_L$ (squares) and exponential fit (solid and dashed lines). For reference, twice the average physical qubit decay is shown (dashed-dotted line). The extracted decay times are indicated on the right. **b**, Corresponding datasets for \hat{X}_L , $|+\rangle_L$ (triangles) and $|-\rangle_L$ (diamonds). For reference, the average physical qubit coherence decay is indicated (dashed-dotted line). **c**, Logical error probability E_L as a function of the number n of error-correction cycles for $|0\rangle_L$ and $|+\rangle_L$ and the extracted error per cycle ϵ_L , indicated on the right. Same symbols as in **a** and **b**. The dashed-dotted line shows the physical two-qubit gate error accumulated over n cycles, for reference. The inset shows simulation results for ϵ_L in state $|0\rangle_L$ (green open circles) for an assumed homogeneous distribution of decoherence rates and gate and readout errors, reduced by factors of $x = 2, 5$ and 10 ; see text for details. The green solid line is a fit to $1/x^2$. QEC, quantum error correction.

provide an upper bound for the performance achievable with the specified device parameters, as further error sources such as gate control errors, population loss into microscopic defect modes and measurement-induced dephasing are not included in the simulation model.

Because the numerical simulations model the performance of our quantum device well, we use the model to project how future improvements in gate and readout fidelities are expected to reduce the logical error per cycle ϵ_L . To free the projection from device-specific spread in qubit parameters, we use the average over all 17 qubits as uniform parameters (see Supplementary Information Table 1) and find good agreement with the results obtained from the qubit-specific model.

We then uniformly reduce all physical error parameters of the numerical model by a factor x , repeat the simulations of $\langle \hat{X}_L \rangle$ and $\langle \hat{Z}_L \rangle$ versus n and extract the mean logical error per cycle ϵ_L as a function of the improvement factor x . We find that the simulated error per cycle scales to a good approximation as $1/x^2$ (see inset in Fig. 4c), as expected for a distance-three code⁴⁴. For reference, we plot the scaled two-qubit physical error per cycle ϵ_{2Q} in the same plot (dashed-dotted line).

A metric commonly used to assess the performance of quantum error correction compares the logical error per cycle ϵ_L to the dominant error on the physical level, typically the two-qubit gate error ϵ_{2Q} (refs. 10,48). Such a comparison is particularly relevant in architectures in which the logical two-qubit gate error is dominated by errors ϵ_L in the quantum error-correction cycles belonging to or following the logical two-qubit gate operation. The number of required cycles scales in general with d in planar architectures and in architectures allowing for transversal execution of logical two-qubit gates^{5,6,23,49,50}. The good agreement between measured (about 3%) and simulated (about 2%) logical errors ϵ_L together with their simulated quadratic scaling suggests that the break-even of per-cycle logical errors with two-qubit gate errors may be in reach for modest improvements of device performance, when using leakage detection or correction.

While a comparison with the break-even point evaluates performance for a fixed code distance d , a comparison related to the error threshold is necessary to judge how far one is from reaching the desired sub-threshold regime, in which ϵ_L decreases exponentially with d . In fact, simulations on the basis of a simplified one-parameter circuit noise model^{44,51} predict a few percent logical error per cycle at threshold, a rate that is close to the logical error per cycle observed in our experiment.

In our experiments, we demonstrate the viability of realizing quantum error correction in the surface code by detecting errors during the error-correction cycle and decoding the error syndromes and correcting for errors in post-processing, which is sufficient in a quantum memory setting. Next-generation experiments will provide the capability of correcting errors during the cycle using real-time decoding¹⁰ and fast in-sequence feedback³⁶, implemented with dedicated digital electronics. Feedback will also enable the mid-cycle suppression of leakage⁵², for example, by auxiliary qubit reset. Realizing larger surface code lattices while improving the performance of their components and demonstrating exponential suppression of logical errors with increasing code distance are upcoming important steps towards achieving the long-term goal of fault-tolerant quantum computation.

Online content

Any methods, additional references, Nature Research reporting summaries, source data, extended data, supplementary information, acknowledgements, peer review information; details of author contributions and competing interests; and statements of data and code availability are available at <https://doi.org/10.1038/s41586-022-04566-8>.

1. Preskill, J. Quantum computing in the NISQ era and beyond. *Quantum* **2**, 79 (2018).
2. Shor, P. W. Fault-tolerant quantum computation. In *Proc. 37th Conference on Foundations of Computer Science* 56 pp (IEEE, 1996).
3. Kitaev, A. Y. Fault-tolerant quantum computation by anyons. *Ann. Phys.* **303**, 2–30 (2003).
4. Dennis, E., Kitaev, A., Landahl, A. & Preskill, J. Topological quantum memory. *J. Math. Phys.* **43**, 4452–4505 (2002).
5. Raussendorf, R. & Harrington, J. Fault-tolerant quantum computation with high threshold in two dimensions. *Phys. Rev. Lett.* **98**, 190504 (2007).
6. Bombin, H. & Martin-Delgado, M. A. Quantum measurements and gates by code deformation. *J. Phys. A Math. Theor.* **42**, 095302 (2009).
7. Andersen, C. K. et al. Repeated quantum error detection in a surface code. *Nat. Phys.* **16**, 875–880 (2020).
8. Marques, J. F. et al. Logical-qubit operations in an error-detecting surface code. *Nat. Phys.* **18**, 80–86 (2022).
9. Chen, Z. et al. Exponential suppression of bit or phase errors with cyclic error correction. *Nature* **595**, 383–387 (2021).
10. Ryan-Anderson, C. et al. Realization of real-time fault-tolerant quantum error correction. *Phys. Rev. X* **11**, 041058 (2021).

11. Bravyi, S. B. & Kitaev, A. Y. Quantum codes on a lattice with boundary. Preprint at <https://arxiv.org/abs/quant-ph/9811052> (1998).
12. Wang, C., Harrington, J. & Preskill, J. Confinement-Higgs transition in a disordered gauge theory and the accuracy threshold for quantum memory. *Ann. Phys.* **303**, 31–58 (2003).
13. Gottesman, D. *Stabilizer Codes and Quantum Error Correction*. PhD thesis, California Institute of Technology (1997).
14. Terhal, B. M. Quantum error correction for quantum memories. *Rev. Mod. Phys.* **87**, 307 (2015).
15. Moussa, O., Baugh, J., Ryan, C. A. & Laflamme, R. Demonstration of sufficient control for two rounds of quantum error correction in a solid state ensemble quantum information processor. *Phys. Rev. Lett.* **107**, 160501 (2011).
16. Schindler, P. et al. Experimental repetitive quantum error correction. *Science* **332**, 1059–1061 (2011).
17. Waldherr, G. et al. Quantum error correction in a solid-state hybrid spin register. *Nature* **506**, 204–207 (2014).
18. Kelly, J. et al. State preservation by repetitive error detection in a superconducting quantum circuit. *Nature* **519**, 66–69 (2015).
19. Knill, E., Laflamme, R., Martinez, R. & Negrevergne, C. Benchmarking quantum computers: the five-qubit error correcting code. *Phys. Rev. Lett.* **86**, 5811 (2001).
20. Abobeih, M. H. et al. Fault-tolerant operation of a logical qubit in a diamond quantum processor. Preprint at <https://arxiv.org/abs/2108.01646> (2021).
21. Egan, L. et al. Fault-tolerant control of an error-corrected qubit. *Nature* **598**, 281–286 (2021).
22. Hilder, J. et al. Fault-tolerant parity readout on a shuttling-based trapped-ion quantum computer. *Phys. Rev. X* **12**, 011032 (2022).
23. Horsman, C., Fowler, A. G., Devitt, S. & Meter, R. V. Surface code quantum computing by lattice surgery. *New J. Phys.* **14**, 123011 (2012).
24. Ofek, N. et al. Extending the lifetime of a quantum bit with error correction in superconducting circuits. *Nature* **536**, 441–445 (2016).
25. Hu, L. et al. Quantum error correction and universal gate set operation on a binomial bosonic logical qubit. *Nat. Phys.* **15**, 503–508 (2019).
26. Flühmann, C. et al. Encoding a qubit in a trapped-ion mechanical oscillator. *Nature* **566**, 513–517 (2019).
27. Campagne-Ibarcq, P. et al. Quantum error correction of a qubit encoded in grid states of an oscillator. *Nature* **584**, 368–372 (2020).
28. Bombin, H. & Martin-Delgado, M. A. Optimal resources for topological two-dimensional stabilizer codes: comparative study. *Phys. Rev. A* **76**, 012305 (2007).
29. Tomita, Y. & Svore, K. M. Low-distance surface codes under realistic quantum noise. *Phys. Rev. A* **90**, 062320 (2014).
30. Koch, J. et al. Charge-insensitive qubit design derived from the Cooper pair box. *Phys. Rev. A* **76**, 042319 (2007).
31. Strauch, F. W. et al. Quantum logic gates for coupled superconducting phase qubits. *Phys. Rev. Lett.* **91**, 167005 (2003).
32. DiCarlo, L. et al. Preparation and measurement of three-qubit entanglement in a superconducting circuit. *Nature* **467**, 574–578 (2010).
33. Negirneac, V. et al. High-fidelity controlled-Z gate with maximal intermediate leakage operating at the speed limit in a superconducting quantum processor. *Phys. Rev. Lett.* **126**, 220502 (2021).
34. Krinner, S. et al. Benchmarking coherent errors in controlled-phase gates due to spectator qubits. *Phys. Rev. Appl.* **14**, 024042 (2020).
35. Negnevitsky, V. et al. Repeated multi-qubit readout and feedback with a mixed-species trapped-ion register. *Nature* **563**, 527–531 (2018).
36. Andersen, C. K. et al. Entanglement stabilization using ancilla-based parity detection and real-time feedback in superconducting circuits. *npj Quantum Inf.* **5**, 69 (2019).
37. Bultink, C. C. et al. Protecting quantum entanglement from leakage and qubit errors via repetitive parity measurements. *Sci. Adv.* **6**, eaay3050 (2020).
38. Aliferis, P. & Terhal, B. M. Fault-tolerant quantum computation for local leakage faults. *Quantum Inf. Comput.* **7**, 139–156 (2007).
39. Fowler, A. G. Coping with qubit leakage in topological codes. *Phys. Rev. A* **88**, 042308 (2013).
40. Ghosh, J. & Fowler, A. G. Leakage-resilient approach to fault-tolerant quantum computing with superconducting elements. *Phys. Rev. A* **91**, 020302 (2015).
41. Suchara, M., Cross, A. W. & Gambetta, J. M. Leakage suppression in the toric code. *Quantum Inf. Comput.* **15**, 997–1016 (2015).
42. Varbanov, B. M. et al. Leakage detection for a transmon-based surface code. *npj Quantum Inf.* **6**, 102 (2020).
43. Versluis, R. et al. Scalable quantum circuit and control for a superconducting surface code. *Phys. Rev. Appl.* **8**, 034021 (2017).
44. Fowler, A. G., Mariantoni, M., Martinis, J. M. & Cleland, A. N. Surface codes: towards practical large-scale quantum computation. *Phys. Rev. A* **86**, 032324 (2012).
45. von Burg, V. et al. Quantum computing enhanced computational catalysis. *Phys. Rev. Res.* **3**, 033055 (2021).
46. Babbush, R. et al. Focus beyond quadratic speedups for error-corrected quantum advantage. *PRX Quantum* **2**, 010103 (2021).
47. Nigg, D. et al. Quantum computations on a topologically encoded qubit. *Science* **345**, 302–305 (2014).
48. Trout, C. J. et al. Simulating the performance of a distance-3 surface code in a linear ion trap. *New J. Phys.* **20**, 043038 (2018).
49. Landahl, A. J. & Ryan-Anderson, C. Quantum computing by color-code lattice surgery. Preprint at <https://arxiv.org/abs/1407.5103> (2014).
50. Gutiérrez, M., Müller, M. & Bermúdez, A. Transversality and lattice surgery: exploring realistic routes toward coupled logical qubits with trapped-ion quantum processors. *Phys. Rev. A* **99**, 022330 (2019).
51. Stephens, A. M. Fault-tolerant thresholds for quantum error correction with the surface code. *Phys. Rev. A* **89**, 022321 (2014).
52. McEwen, M. et al. Removing leakage-induced correlated errors in superconducting quantum error correction. *Nat. Commun.* **12**, 1761 (2021).

Publisher's note Springer Nature remains neutral with regard to jurisdictional claims in published maps and institutional affiliations.

© The Author(s), under exclusive licence to Springer Nature Limited 2022

Methods

Parity measurement

In a Z-basis measurement, if an odd number of the data qubits involved in the parity operator under consideration is in the $|1\rangle$ state, the auxiliary qubit state is flipped. On the other hand, if an even number of data qubits is in $|1\rangle$, the auxiliary qubit state remains unchanged. The equivalent is true in the X basis for an even or an odd number of data qubits in the $|-\rangle$ state. Here $|0\rangle$ and $|1\rangle$ are the transmon qubit ground and first excited states, respectively, and $|\pm\rangle = (|0\rangle \pm |1\rangle)/\sqrt{2}$ are their superpositions. To map the parity of the data qubits D_j onto the corresponding auxiliary qubit, we effectively use a sequence of controlled-NOT gates with the data qubits as control and the auxiliary qubit as target, and subsequently measure the state of the auxiliary qubit in the Z basis using single-shot readout. In the Z basis, a single bit-flip error of any individual data qubit leads to a change of parity, as does a single phase-flip in the X basis. Hence measurements of changes of data-qubit parities allow us to detect and identify phase-flip or bit-flip errors, as long as they occur sufficiently rarely⁴⁴.

CZ gates

We realize the necessary two-qubit CZ gates by tuning adjacent pairs of data (D_j) and auxiliary qubits (X_i, Z_i) into resonance^{31–33} using individual flux lines implemented with coplanar waveguides (green in Fig. 1b) shorted near the superconducting quantum interference device (SQUID) loop of each qubit. We fabricated all qubits with asymmetric SQUIDs^{53,54} to allow for data qubits to idle at their minimum and auxiliary qubits at their maximum frequencies, at which the qubits are first-order insensitive to flux noise. Data qubits are designed with idle frequencies 3.7–4.1 GHz in a low-frequency band and auxiliary qubits with idle frequencies 5.9–6.3 GHz in a high-frequency band (red and blue/green dots in Fig. 1c); also see Supplementary Information (section II).

We implement CZ gates by tuning both data and auxiliary qubits to an intermediate interaction frequency ω_{int} and $\omega_{\text{int}} - \alpha$, respectively, with $\omega_{\text{int}}/2\pi$ ranging from 4.4 to 5.6 GHz (Supplementary Information, section III). The qubit anharmonicity $\alpha \approx -0.17$ GHz is designed to be small to minimize residual qubit–qubit interactions³⁴. We make use of net-zero flux pulses³³, which reduce both the detrimental effect of low-frequency flux noise on qubit coherence and the impact of non-idealities in the transfer function of the flux lines on gate fidelities. Given the large designed detuning of about 2 GHz between the data and auxiliary qubits at their idle frequencies, we calculate residual ZZ interaction strengths between qubits lower than $\alpha_{\text{zz}}/2\pi \approx 8$ kHz (ref. ³⁴). It is only during two-qubit gate execution that α_{zz} increases by a factor of approximately 2 to 25, depending on the interaction frequency ω_{int} , which we partially mitigate using echo pulses. The coupling strength between auxiliary qubits and data qubits at the interaction point is about $J/2\pi \approx 7$ MHz.

Two-qubit gate error

We determine the two-qubit gate error from interleaved randomized benchmarking experiments with sets of three gates executed in parallel, as used in our realization of the surface-code cycle. Time-varying microscopic defects in our device have a detrimental influence on two-qubit gate performance and are responsible for outliers in the gate-error distribution (Supplementary Information, section III).

Qubit readout

Each qubit is coupled to a resonant pair of readout resonator and Purcell filter (red and blue $\lambda/4$ coplanar waveguide resonators in Fig. 1b). Moreover, each readout resonator is coupled strongly to the qubit ($g/2\pi \approx 169$ MHz for auxiliary qubits and $g/2\pi \approx 252$ MHz for data qubits) and has a large effective bandwidth ($\kappa_{\text{eff}}/2\pi \approx 10$ MHz) to enable fast, high-fidelity readout⁵⁵. The individual Purcell filters both maintain

high qubit coherence, despite the large coupling and bandwidth of the readout resonators, and reduce undesired readout crosstalk (Supplementary Information, section V) between qubits that are in close proximity or have similar frequencies⁵⁶. This is particularly important for the simultaneous frequency-multiplexed readout of groups of four or five qubits using joint feed lines (purple coplanar waveguides in Fig. 1b). The readout resonator frequencies are separated by about 200 MHz within each feed line and occupy a frequency band extending from 6.8 to 7.6 GHz (purple points in Fig. 1c).

We read out the states of all qubits dispersively by applying frequency-multiplexed, Gaussian-filtered microwave pulses of duration 200–300 ns to all four feed lines. We integrate the transmitted signals in a heterodyne detection scheme for a duration of 400 ns (Supplementary Information, section VI). Auxiliary qubits are read out near their idle frequencies, whereas data qubits are read out at a flux-tuned qubit frequency of approximately 5 GHz, reducing the data-qubit-readout resonator detuning⁵⁷ and thus enhancing the dispersive coupling and the readout fidelity^{55,58}.

Gate sequence

The two-qubit gates are accompanied by a set of single-qubit gates applied to all auxiliary qubits in a leading and a trailing time step, and a dynamical decoupling pulse applied to all data qubits at a central time step (Fig. 3a). We choose the order of gate operations to provide resilience against single auxiliary qubit errors and to avoid interactions with microscopic defect modes (Supplementary Information, section III).

Leakage detection

We make use of a leakage-detection scheme on the basis of three-state readout, which allows us—in post-processing—to reject those sequences in which any of the qubits were measured in a leakage state; see Supplementary Information (section VI). In our CZ gate scheme, we make use of the second excited state $|2\rangle$ of the auxiliary qubits rather than that of the data qubits to mediate the interaction, which minimizes data qubit leakage. Performing three-state readout of the data qubits after the final error-correction cycle, we reject experimental runs for which data qubit leakage was detected. The rejected fraction per qubit and per cycle amounts to 0.0017(2). In addition, there is a cycle-independent rejection probability of about 0.01 per qubit, owing to false positives caused by readout error. In addition, we detect if any of the eight auxiliary qubits has leaked to the $|2\rangle$ state in any of the n cycles, using the same three-state readout, and find an average rejection probability of 0.0094(4) per qubit per cycle. In total, this leads to a rejected data fraction per cycle of 8%.

Logical-state characterization

For the data shown in Fig. 3b, we use our leakage-detection scheme and correct for readout errors on data qubits. The logical fidelity is calculated as $F_L = F_{\text{phys}}/P_L = 99.6(2)\%$, in which $P_L = 54.2(1)\%$ is the experimentally measured probability of preparing a state in the logical subspace (Supplementary Information, section IX). Both F_{phys} and P_L are smaller than in a distance-two surface code (see ref. ⁷ for an example) because the two quantities are expected to decrease with increasing distance d at a constant physical error rate. To further evaluate the performance of our logical-state initialization, we analyse the fidelity of the prepared state with respect to subspaces of states that our surface-code implementation can, in principle, correct. The errors that are correctable by the distance-three surface code include all single-qubit Pauli (weight-one) errors \hat{X}_j, \hat{Y}_j or \hat{Z}_j on any data qubit j and a subset of higher-weight errors; see Supplementary Information (section IX) for details. We observe that weight-one errors account for most of the errors on data qubits in the $|0\rangle_L$ state initialization, with higher-weight errors having a largely reduced probability of occurrence (see Fig. 3b).

Syndrome graph

For syndrome analysis, we construct a graph in which the syndrome elements are shown at the auxiliary qubit locations along two spatial coordinates for each cycle index m , which forms the temporal coordinate. Spatial and temporal correlations between non-zero syndrome elements correspond to data and auxiliary qubit errors, respectively. If the overall error rate is sufficiently low, we obtain a low density of non-zero syndrome elements, or – equivalently – mean syndrome element values $\bar{\sigma}_m^{Ai} \ll 1$, with the mean taken over experimental realizations. In that case, the underlying errors can be decoded with low ambiguity (Supplementary Information, section XII).

Syndrome analysis

All syndrome elements $\bar{\sigma}_m^{Ai}$ averaged over repetitions of the experiments are approximately constant as a function of m for $m \geq 2$; see Fig. 3c, d obtained for preserving $|0\rangle_L, |1\rangle_L$ and $|+\rangle_L, |-\rangle_L$, respectively. We attribute the small remaining increase of $\bar{\sigma}_m^{Ai}$ with m to the fact that, in the absence of auxiliary qubit reset, auxiliary qubits initially prepared in the ground state tend to an asymptotic probability of 0.5 to be in the excited state after m cycles. As a result, with increasing m , auxiliary qubits suffer from larger decoherence during readout and during the subsequent idling periods of about 150 ns before the start of the next quantum-error-correction cycle. Our numerical simulations show the same feature (open symbols in Fig. 3c, d). For $m = 1$, the averaged syndrome elements $\bar{\sigma}_1^{Ai}$ are reduced because the corresponding reference stabilizer values are computed from the initial data qubit product state, which we prepare with high fidelity. In the first cycle, the four values of $\bar{\sigma}_1^{Zi}$ are smaller than $\bar{\sigma}_1^{Xi}$ because a quantum-error-correction cycle starts with measurements of \hat{S}^{Zi} and errors thus accumulate only during half a cycle.

Error decoding

We decode the error syndromes using a minimum-weight perfect-matching algorithm^{59,60}. We determine the weights in an error-model-free approach by inferring the errors per cycle from the measured data using a correlation analysis of the syndromes as described in the Supplementary Information (section XII) and refs.^{9,61}. The correction of an error, initiated by analysing all cycles in post-processing, takes the form of changing the sign of the logical qubit operator values z_L and x_L when indicated by the decoder. We note that, for correcting \hat{Z}_L , it is sufficient to decode only syndromes $\{\sigma_m^{Zi}\}$, or – equivalently – only $\{\sigma_m^{Xi}\}$ for \hat{X}_L .

Logical coherence times

The reference for the logical energy relaxation time T_{1L} is twice the mean physical qubit energy relaxation time T_1 , assuming an infinite lifetime of the physical qubit ground state for the comparison.

We also note that, within error bars, the lifetimes of the states $|0\rangle_L$ and $|1\rangle_L$, and the coherence times of the states $|+\rangle_L$ and $|-\rangle_L$ are, respectively, identical. This is expected, as all cardinal states of the logical qubit have the same number of qubits in the excited state and as our dynamical decoupling scheme alternates between the states $|0\rangle_L$ and $|1\rangle_L$, and between the states $|+\rangle_L$ and $|-\rangle_L$, respectively, which are therefore affected similarly by decoherence.

To compare the performance of the error-correction experiments presented here to the recent error-detection experiments in distance-two surface codes realized with seven qubits^{7–9}, we post-select data from those runs of our distance-three experiment in which all syndrome elements are zero. When doing so, we estimate logical lifetimes in excess of 1 ms (Supplementary Information, section XIII). In

the seven-qubit device, logical lifetimes and coherence times in the range 60–70 μ s were observed, with comparable data-retention rates of about 50% per cycle when post-selecting on no detected errors by evaluating three stabilizers⁷. The current 17-qubit device achieves similar data-retention rates when evaluating eight stabilizers per cycle. This observation demonstrates that our 17-qubit device, including the tune-up and calibration procedures used, performs notably better than our previous seven-qubit device.

Data availability

All data are available from the corresponding author on reasonable request.

- Strand, J. D. et al. First-order sideband transitions with flux-driven asymmetric transmon qubits. *Phys. Rev. B* **87**, 220505 (2013).
- Hutchings, M. D. et al. Tunable superconducting qubits with flux-independent coherence. *Phys. Rev. Appl.* **8**, 044003 (2017).
- Walter, T. et al. Rapid high-fidelity single-shot dispersive readout of superconducting qubits. *Phys. Rev. Appl.* **7**, 054020 (2017).
- Heinsoo, J. et al. Rapid high-fidelity multiplexed readout of superconducting qubits. *Phys. Rev. Appl.* **10**, 034040 (2018).
- Sank, D. et al. Measurement-induced state transitions in a superconducting qubit: beyond the rotating wave approximation. *Phys. Rev. Lett.* **117**, 190503 (2016).
- Wallraff, A. et al. Approaching unit visibility for control of a superconducting qubit with dispersive readout. *Phys. Rev. Lett.* **95**, 060501 (2005).
- O'Brien, T. E., Tarasinski, B. & DiCarlo, L. Density-matrix simulation of small surface codes under current and projected experimental noise. *npj Quantum Inf.* **3**, 39 (2017).
- Edmonds, J. Paths, trees, and flowers. *Can. J. Math.* **17**, 449–467 (1965).
- Spitz, S. T., Tarasinski, B., Beenakker, C. W. J. & O'Brien, T. E. Adaptive weight estimator for quantum error correction in a time-dependent environment. *Adv. Quantum Technol.* **1**, 1800012 (2018).

Acknowledgements We are grateful for valuable discussions with Q. Ficheux and C. Lledó. We acknowledge the contributions of R. Boell to the experimental setup and M. Kerschbaum for early work on the two-qubit gate implementation. The team in Zurich acknowledges financial support by the Office of the Director of National Intelligence (ODNI), Intelligence Advanced Research Projects Activity (IARPA), through the U.S. Army Research Office grant W911NF-16-1-0071, by the EU Flagship on Quantum Technology H2020-FETFLAG-2018-03 project 820363 OpenSuperQ, by the National Center of Competence in Research ‘Quantum Science and Technology’ (NCCR QSIT), a research instrument of the Swiss National Science Foundation (SNSF, grant number 51NF40-185902), by the SNSF R’Equip grant 206021-170731, by the EU programme H2020-FETOPEN project 828826 Quomorphic and by ETH Zurich. S.K. acknowledges financial support from Fondation Jean-Jacques et Félícia Lopez-Loreta and the ETH Zurich Foundation. The work in Sherbrooke was undertaken thanks in part to funding from NSERC, Canada First Research Excellence Fund, ARO grant W911NF-18-1-0411, the Ministère de l’Économie et de l’Innovation du Québec and U.S. Department of Energy, Office of Science, National Quantum Information Science Research Centers, Quantum Systems Accelerator. M.M. acknowledges support by the U.S. Army Research Office grant W911NF-16-1-0070. The views and conclusions contained herein are those of the authors and should not be interpreted as necessarily representing the official policies or endorsements, either expressed or implied, of the ODNI, IARPA or the U.S. Government.

Author contributions S.K., N.L. and A.R. planned the experiments, S.K. and N.L. performed the main experiment and S.K. and N.L. analysed the data. F.S., A.R. and C.K.A. designed the device and S.K., A.R. and G.J.N. fabricated the device. N.L., C.H. and S.L. developed the experimental software framework and A.R., C.H., N.L., S.K. and S.L. developed the control and calibration software routines. A.R., J.H., S.K. and C.H. designed and built elements of the room-temperature setup and S.K., A.R., C.H., S.L., N.L. and F.S. maintained the experimental setup. S.K., N.L., A.R., C.H., S.L. and C.K.A. characterized and calibrated the device and the experimental setup. E.G., A.D.P. and C.L. performed the numerical simulations. M.M. provided guidance on logical qubit evaluation methodology aspects. S.K., N.L., A.R., C.H. and S.L. prepared the figures for the manuscript and S.K., N.L., A.R., C.E. and A.W. wrote the manuscript, with inputs from all co-authors. A.B., C.E. and A.W. supervised the work.

Competing interests The authors declare no competing interests.

Additional information

Supplementary information The online version contains supplementary material available at <https://doi.org/10.1038/s41586-022-04566-8>.

Correspondence and requests for materials should be addressed to Sebastian Krinner.

Peer review information Nature thanks Kyungjoo Noh and the other, anonymous, reviewers for their contribution to the peer review of this work.

Reprints and permissions information is available at <http://www.nature.com/reprints>.